Retrospective Detection and Suppression of Dark-Rim Artifacts in First-Pass Perfusion Cardiac MRI Enabled by Deep Learning

Hazar Benan Unal, Taylor Beaulieu, Luis Zamudio Rivero, Rohan Dharmakumar, Behzad Sharif,
Member, IEEE

Abstract—The dark-rim artifact (DRA) remains an important challenge in the routine clinical use of first-pass perfusion (FPP) cardiac magnetic resonance imaging (cMRI). The DRA mimics the appearance of perfusion defects in the subendocardial wall and reduces the accuracy of diagnosis in patients with suspected ischemic heart disease. The main causes for DRA are known to be Gibbs ringing and bulk motion of the heart. The goal of this work is to propose a deep-learning-enabled automatic approach for the detection of motion-induced DRAs in FPP cMRI datasets. To this end, we propose a new algorithm that can detect the DRA in individual time frames by analyzing multiple reconstructions of the same time frame (k-space data) with varying temporal windows. In addition to DRA detection, our approach is also capable of suppressing the extent and severity of DRAs as a byproduct of the same reconstruction-analysis process. In this proof-of-concept study, our proposed method showed a good performance for automatic detection of subendocardial DRAs in stress perfusion cMRI studies of patients with suspected ischemic heart disease. To the best of our knowledge, this is the first approach that performs deep-learning-enabled detection and suppression of DRAs in cMRI.

Clinical Relevance— Our approach enables clinicians to provide a more accurate diagnosis of ischemic heart disease by detecting and suppressing subendocardial dark-rim artifacts in first-pass perfusion cMRI datasets.

I. INTRODUCTION

First-pass perfusion (FPP) cardiac magnetic resonance imaging (cMRI) has been established as a validated technique to detect myocardial ischemia and hemodynamically significant coronary artery disease [1-4]. Visual inspection of FPP cMRI is usually the preferred clinical method to detect the perfusion defects in patients with suspected ischemic heart disease. However, the effectiveness of FPP cMRI can often be limited by a notorious image artifact called "dark-rim artifact" (DRA). DRA appears as a dark band or rim along the subendocardial border of the left ventricular (LV) cavity in the FPP time series. It is most visible when there is a sharp transition in signal intensity between the blood pool and myocardium. An example of DRA is shown in Fig. 1.

DRA can easily hide or mimic the true perfusion defects which also appear darker than the surrounding myocardium. Unlike true perfusion defects, DRAs generally disappear after several frames following the peak LV-enhancement phase, and therefore could be distinguished by expert readers by careful examination of their spatio-temporal behavior. However, subjective interpretation of FPP cMRI image series can lead to variabilities between different readers and inaccurate diagnosis [5]. In addition to the challenges that DRA creates for visual (qualitative) assessment of cMRI data, it can also cause significant errors in the quantified myocardial blood flow by influencing the temporal behavior of signal intensity in subendocardial pixels [6, 7]. For these reasons, it is important to have the necessary information about the presence of DRA in FPP cMRI image series in order to enable accurate and reliable diagnosis.

DRA is known to be primarily caused by two contributing factors: (a) Gibbs ringing due to truncated coverage of k-space especially in Cartesian-sampled protocols [6], and (b) the bulk motion of the heart [8]. Gibbs ringing is a general problem in cMRI studies because of the practical requirement to exclude some of the high-frequency content (i.e., truncation) in k-space during data acquisition. This phenomenon can be characterized using point spread function (PSF) analysis [6,12]. On the other hand, motion-induced DRA occurs because of a similar PSF effect [8].

In the past decade, several techniques have been proposed that attempt to suppress or eliminate the DRA by post-processing [9, 10] or using optimized data acquisition including non-Cartesian sampling of k-space [11-13]. However, these techniques primarily focus on Gibbs-ringing-induced DRA rather than motion-induced DRA. Moreover, they do not provide any information about the likely location of DRA in a specific FPP image. Recently, Ta et al. suggested using pixel-wise fully-quantitative myocardial blood flow analysis to differentiate regions with DRA from true perfusion defects [14]. However, fully quantitative assessment of blood flow is currently not performed in a majority of clinical scenarios, which limits the applicability of this approach in routine clinical settings, i.e., outside of research-focused medical centers.

In this work, we propose a new deep-learning-enabled methodology that can automatically detect motion-induced DRA in a wide range of perfusion cMRI datasets by performing multiple reconstructions of the FPP cMRI image series (acquired k-space data) with different temporal

H. Unal, T. Beaulieu, L. Zamudio, and B. Sharif are with Cedars-Sinai Medical Center, UCLA Dept. of Bioengineering, and the Laboratory for Translational Imaging of Microcirculation, Krannert Cardiovascular Research Center, Indiana University School of Medicine, Indianapolis (corresponding author: Behzad Sharif, PhD; phone: 310-423-7758; e-mail: behzad.sharif@cshs.org, bzsharif@gmail.com).

R. Dharmakumar is with the Krannert Cardiovascular Research Center, Dept. of Medicine, and IU Health/IUSM Cardiovascular Institute, Indiana University School of Medicine, Indianapolis.

windows, which influences the presence and severity of motion-induced DRAs. We employ a 3D convolutional neural network (CNN) to automatically detect the subendocardial layer and use this segmentation to tease out the effect of cardiac motion at a pixel level. To this end, for each time frame, myocardial regions that are reconstructed with different temporal windows are stacked, and pixel-wise slopes along the "reconstruction dimension" are computed. A byproduct of this approach is the ability to obtain a modified reconstruction of the same dataset that may result in reduced DRA.

II. METHODS

A. Motion-induced Dark-Rim Artifacts

In a previous study[8], bulk motion of the heart is shown to result in a similar PSF of that of k-space truncation. Reconstructed image can be described as a convolution of underlying true image and the motion-induced PSF:

$$I_v = |\rho_v| = |\rho_0 * \psi_m| \qquad (1)$$

where ρ_0 is the true image and ψ_m is the PSF due to motion. After analytical calculation of PSF for given parameters (field of view, velocity, number of readouts, duration etc.) with the assumption of constant 1-D motion, the study shows that the length scale of DRA is proportional to width(W) of the main lobe of this PSF which is calculated by

$$W_{main} = \sqrt{2X_{ph}v\tau} \qquad (2)$$

where X_{ph} is field of view (FOV) along phase-encode direction, v is velocity and τ is time elapsed during acquisition. This equation suggests that fast motion and longer temporal window result in an increased severity of DRA.

Although this is an oversimplified formulation for much more complicated motion characteristics of the heart (3D non-rigid motion, rotation, contraction etc.), (2) demonstrates that velocity and temporal window play the main role in the characteristics of motion-induced PSF. Based on this, our approach uses this difference in motion characteristics at different parts of k-space to detect which myocardium segments have DRA.

To verify that using different parts of k-space results in different motion-induced DRA, we did dynamic numerical simulations that mimic systole and diastole phases of cardiac cycle. The dynamic numerical phantom is prepared by dividing k-space into 7 divisions and filling each division with k-space from a different snapshot of the phantom heart. Fig. 2 visualizes this procedure with 5 k-space divisions for simplicity.

B. Data Acquisition

Typical data acquisition in FPP cMRI includes an ECG signal for cardiac gating, a Saturation-Recovery (SR) pulse for magnetization preparation, and a Gradient Echo (GRE) pulse sequence to fill k-space of one frame from each slice as explained in Fig. 2. Usually, 3 slices from the heart are acquired between 2 heart beats. Depending on the repetition time (TR) and total number of readout lines ($N_{readout}$), the full temporal window for each frame can vary between 60ms-150ms. The amount of motion captured during the temporal
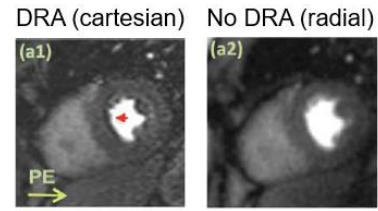

Figure 1. **An example of a subendocardial dark-rim artifact (DRA) in first-pass perfusion (FPP) cardiac MRI (cMRI).** (a1): a time-frame from FPP cMRI image series with Cartesian acquisition. As highlighted by the red arrow, there is a DRA in septal wall along the phase-encode (PE) direction, which could be confused with a true perfusion defect. Panel (a2) shows the ground-truth for the same time-frame, which does not have a DRA due to the properties of the point spread function of radial k-space acquisition.

window determines the characteristics of motion-induced DRA (e.g. width, intensity, dip amplitude etc.) as described in the previous section.

It should be noted that motion characteristics are different in each cardiac phase as heart keeps contracting/relaxing during data acquisition. As shown with cartoon image of heart in Fig. 2, the left side (i.e. the beginning of k-space) and the right side (i.e. the ending of k-space) collect data from slightly different cardiac phases. For example, the diameter of blood pool and thickness of myocardium are different at the beginning and ending of systole phase. Moreover, the rate of change is larger at the beginning of contraction, which contributes more to the motion-induced DRA in the reconstructed image with full temporal window. This prior information will be used during processing of slope maps in the proposed workflow.

C. Automated Myocardium Segmentation with 3D CNN

Since DRAs occur within the myocardium, it is important to extract this region of interest (ROI) with a fast and effective method to narrow down the potential location of DRA in the reconstructed images. We used a 3D CNN technique previously proposed by our group [15] due to its ability for fast and accurate segmentation. The network also outputs two right
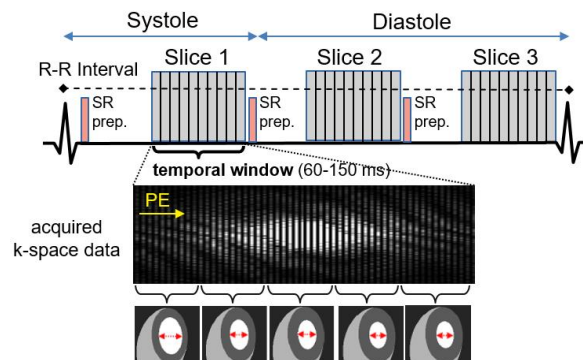

Figure 2. **Typical data acquisition in a FPP cMRI study**. 3 slices are acquired between 2 heart beats in an undersampled way for faster acquisition. Each slice is SR-prepared and a cartesian FLASH sequence is used to fill the k-space. Acquiring k-space data for one frame takes 60 ms to 150 ms. As shown with cartoon images, the heart keeps moving as k-space is being filled. This motion results in DRA whose characteristics are dependent on the type and amount of the motion. Contraction is exaggerated in cartoon images for better visualization.
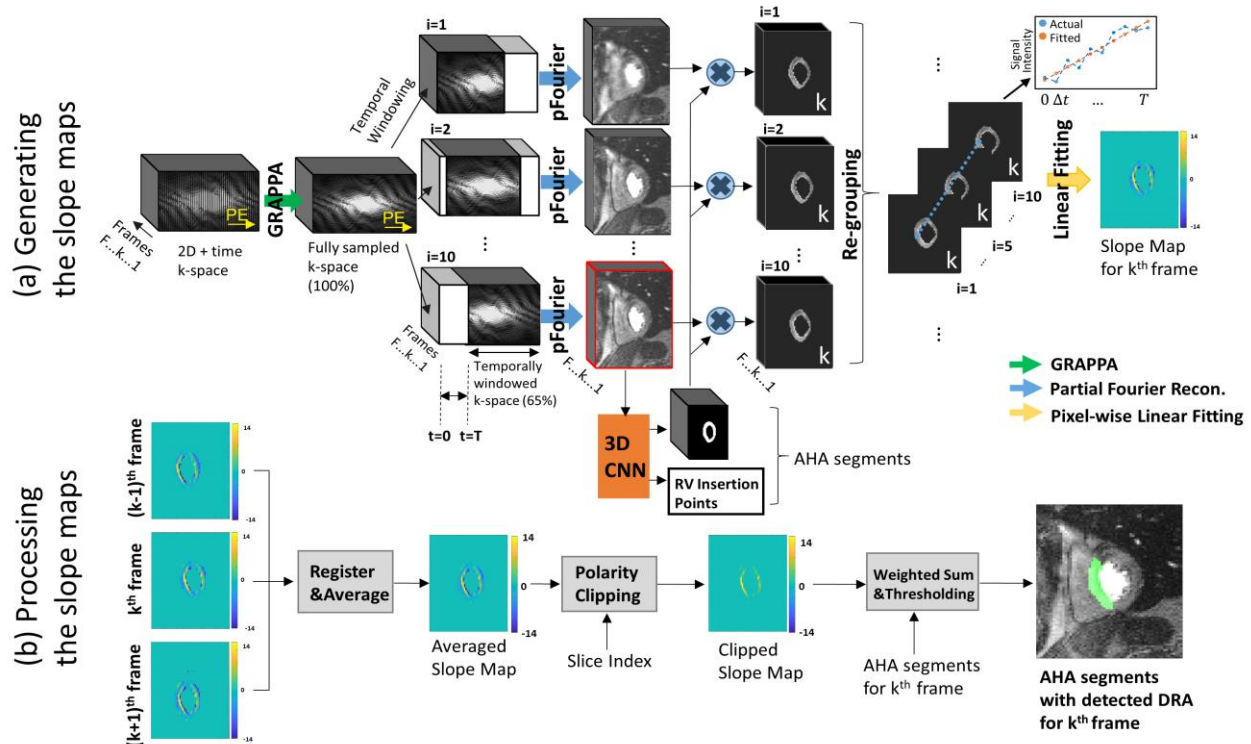
Figure 3. **Description of the proposed algorithm for DRA detection in myocardial segments (6-segment AHA model)**. The workflow is explained in 2 modules. (a) Generating the slope maps for each frame. Acquired undersampled k-space data with F frames are reconstructed to the fully sampled k-space data with GRAPPA. Each frame in full k-space is temporally windowed with 10 different windows with width equal to 65% of full k-space. The time difference T between two extreme windows is therefore 35% of total temporal window. Each new k-space is then reconstructed into image frames with partial Fourier reconstruction algorithm. One of these 2D+time reconstructions (highlighted with red contour) is input to the 3D CNN which outputs myocardial segmentations and RV insertion points [15]. RV insertion points are used to divide myocardium masks into 6 AHA segments. 2D+time myocardium masks are multiplied with each realization to extract myocardium regions. After that, these 2D+time images are re-grouped such that each frame that is reconstructed with a different temporal window is stacked together (only an arbitrary k^{th} frame is shown for simplicity). For each pixel, data points along the 3rd dimension are fitted into a linear line by also accounting for the time difference between each realization. These pixel-wise slope values give the "slope map" for each frame. (b) Processing the slope maps. Slope maps from 2 neighboring frames are registered to the frame of interest, and these 3 slope maps are averaged. By using the prior information about which slice that frame belongs to, slope values with either plus or minus polarity are clipped. This clipping gives a clearer slope map by removing the blood pool/partial volume pixels. Finally, each myocardial segment is assigned a score depending on the slope values it contains, and classified as having or not having DRA.

ventricle (RV) insertion points, which allows for automatic segmentation of myocardium in the FPP image series.

D. Proposed Workflow

The main idea of our algorithm relies on the gradual changes in motion characteristics of the acquired data from one side of k-space to the other. By investigating the behavior of each pixel for different temporal windows, we can gather information about the location of DRA. The proposed algorithm is summarized in Fig. 3.

The first step of the algorithm is to obtain the full k-space from undersampled data by using a parallel imaging technique such as GRAPPA [16]. As described earlier, reconstructing the frames with full (i.e. 100%) temporal window captures more amount of motion. This means that the motion characteristics at the beginning and the ending of k-space are averaged during conventional reconstruction.

After that, the full k-space is windowed by 10 different temporal windows (with temporal width of 65% of full k-space) with a sliding window approach. As these windowed k-spaces contain data from different time stamps of acquired data, each of these 10 versions will have different motion characteristics and different motion-induced DRA.

Each windowed k-space is then reconstructed into corresponding 2D+time image series by applying partial Fourier reconstruction. Each reconstructed image series with a different temporal window is called a "realization". To obtain ROI for each frame, one of the image series is input to the 3D CNN myocardium segmentation network. It is sufficient to use output masks from any one of the realizations since the reconstructed images with different temporal windows do not differ from each other significantly in terms of location of myocardium since the total motion is generally at subpixel level. Myocardium from each image series is extracted by multiplying the masks with each 2D+time realization. As 3D CNN network will also output the RV insertion points, we will be able to divide the myocardium into 6 AHA segments by using these insertion points when processing the slope maps.

Then, the same frames that are reconstructed with different temporal windows are stacked along 3rd dimension. Each frame in the stack is normalized to the average of 95% percentile of blood pool pixels in that frame. For each pixel, signal intensity change along 3rd dimension is fit into a linear

line. By taking the slope value for each pixel after the linear fitting, pixel-wise slope map for that frame is generated. To account for different acquisition times, time interval for the data points is set to the time difference between left-most and right-most temporal windows, which can be found by $0.35 \times TR \times N_{readout}$. The purpose of finding the slope maps is to find out which pixels have a clear trend towards getting darker or brighter as temporal window is being shifted from one side of k-space to the other. Since the value of a normal non-DRA pixel is not expected to be affected by different temporal windows as remarkably as a motion-induced DRA pixel, large-amplitude slope values will be an indication of that particular pixel belonging to a DRA. Similarly, pixels that belong to normal tissue or a perfusion defect will have small or zero slope values.

Since DRAs do not appear in one frame and completely disappear in the next frame, we can incorporate this temporal behavior of DRA to increase the robustness of the detection algorithm. To do this, we register the slope maps from neighbor frames into the slope map of the frame of interest, and take the average of the registered slope maps. The advantage of this step is that it preserves the DRA features that repeat in successive frames, and suppresses the noise-like high slope values that are not consistently observed in neighboring frames.

One of the prior knowledge we can use to further clean the slope maps is based on the motion of the heart in different cardiac phases. As described in Data Acquisition section, typical FPP cMRI sequence acquires 3 slices. Slice 1 is acquired when the heart is primarily in the systole phase, where it contracts rapidly at the beginning of k-space and slows down towards end-systole. This means that the left-side of k-space captures more rapid motion and results in more severe DRA. As a result, DRA pixels in Slice 1 are expected to be darker when the temporal window is close to the left-side of k-space. Therefore, the slope values for DRA pixels should be positive as the reconstructed pixel value will be increasing from left to the right k-space. Similarly, Slice 2 and 3 are acquired in diastole, where the heart relaxes and LV cavity expands during acquisition. Oppositely to Slice 1, the slope
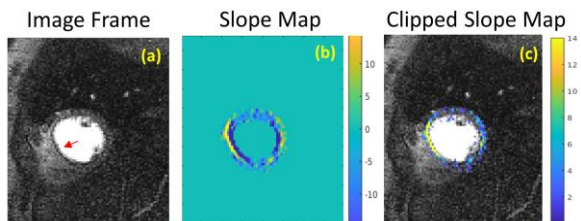
values for DRA pixels in Slice 2 and 3 will be negative. For this reason, slopes with a certain polarity can be clipped depending on which slice the frame of interest belongs to. The effect of clipping is shown in Fig. 4. A byproduct of this prior information about cardiac phases is the ability to remove/suppress DRA from the reconstructed images by using the k-space portion that captures less motion for that slice. This is demonstrated in more detail in the Results section.

The final step is the processing of the final slope map to detect the myocardial segments with DRA. We classify a myocardial segment as having or not having a DRA depending on a score calculated based on weighted average of number of "bright" pixels inside that segment. Very bright pixels that exceed a certain threshold are weighted by 4, moderately bright pixels that exceed a lower threshold are weighted by 1, and all pixels that are smaller than the lower threshold are weighted by 0. After calculating the score for each myocardial segment, segments that have a score higher than 11 are classified as having DRA. Otherwise, they are classified as not having DRA. These threshold values are determined experimentally.

The proposed algorithm is applied to 15 volunteer studies as well as large animal studies (2 canines). For all of the volunteer and patient imaging studies, local Institutional Review Board (IRB) approval and written informed consent was obtained before each imaging exam/study. Imaging experiments in animals were done under a protocol approved by the local Institutional Animal Care and Usage Committee. Three slices from each human study and 1 slice from each canine study were used (47 slices in total).

III. RESULTS

A. DRA Reduction by Temporal Windowing

As described in the earlier sections, the severity of DRA depends on motion characteristics during the acquisition of k-space. Since we have the prior knowledge about the cardiac phases in which each slice is acquired, we can estimate which portion of k-space might contribute to motion-induced DRA.

Figure 4. **Description of a "clipping" procedure to remove blood pool/partial volume pixels.** (a) An example FPP image frame with DRA in the septal wall. (b) Pixelwise slope map corresponding to changes in pixel values according to 10 reconstructions with a sliding window approach (Section II). Note that there are large-amplitude pixels near the septum with opposite polarities (c) Using the prior knowledge that we have about the behavior of motion-induced DRAs in different slices (Fig. 2), we can ignore the pixels with a certain polarity. This particular frame belongs to Slice 1 (Fig 2), and the prior knowledge we have suggests that pixels with DRA need to have positive slope for Slice 1. As can be seen from the composite image in (c), the clipping procedure gives a more precise slope map wherein the blood pool pixels with large negative slope are removed.
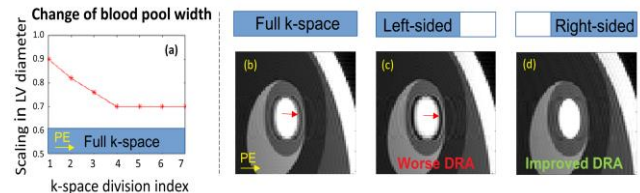

Figure 5. **Dynamic simulation for systolic phase.** (a) For dynamic simulations using a numerical phantom, k-space is filled in 7 temporal steps. To simulate systole, LV diameter scaling (i.e., the ratio of LV cavity diameter to whole LV diameter) decreases linearly when filling the first 4 divisions as shown in panel (a). The last 3 divisions are filled assuming the LV diameter scaling remains the same as heart slows down towards the end of systole. Panel (b) is the conventional reconstruction where all of the acquired k-space is used (full temporal footprint). This results in a clear DRA along the phase-encode direction. Panel (c) shows the reconstruction by using a left-sided temporal window, which in this case includes the k-space portion during contraction. As can be seen, this results in a more severe DRA. Finally, (d) shows the reconstruction by using a right-sided temporal window, which covers the k-space portion where the heart is mostly still. As a result, (d) has less motion-induced DRA.

Since the systolic phase has a rapid contraction at the beginning of data acquisition, using the right side of k-space results in less DRA for Slice 1 (Fig. 2). For the diastole phase, heart is relaxing and using the left side of k-space results in less DRA for Slice 2 and Slice 3 (using the slice-indexing approach shown in Fig. 2).

Fig. 5 shows the results of dynamic numerical simulations for the systolic phase. Fig. 5a explains the motion of the simulated heart during data acquisition: as the k-space lines are filled from left to right, the diameter of LV blood pool first linearly decreases, then remains constant, simulating a contracting heart in systole. Fig. 5b shows the conventional reconstruction which uses the full temporal window. As shown with red arrows, the reconstruction with full temporal window has subendocardial DRA along the phase-encode direction. Fig. 5c is the resulting image when only 65% of k-space data from the left-side of k-space is used for reconstruction. As the left-side captures most of the motion during systole, the reconstructed image has even more severe DRA as shown with red arrows. Finally, Fig. 5d shows the image when 65% of k-space data from the right-side of k-space is used for reconstruction. As the numerical phantom is mostly still while the right-side of k-space is being filled, the resulting image has much less DRA.

Our proposed DRA reduction procedure was tested in human and animal data. As an example case, Fig. 6 shows the reconstructed images from different slices for a healthy
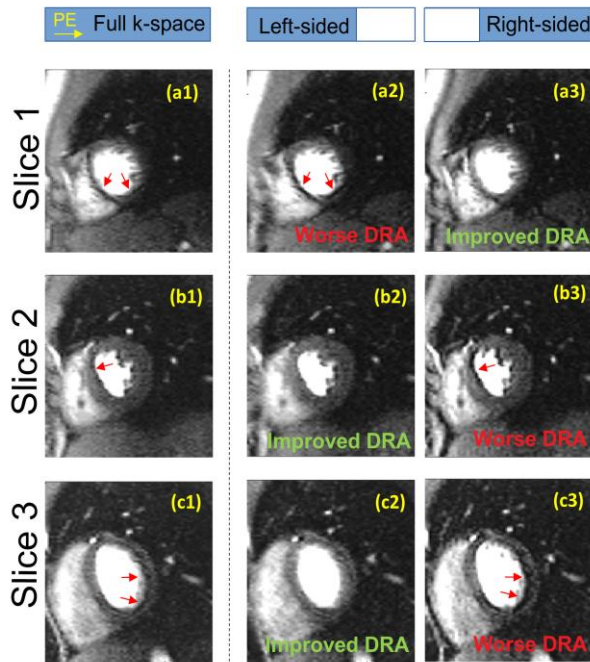

Figure 7. **Representative frame for DRA reduction from a healthy volunteer.** (a) Conventional reconstruction uses the full temporal window in k-space which results in motion-induced DRA throughout the subendocadial wall (red arrows). (b) Proposed approach for DRA reduction uses the temporally windowed k-space with less motion. As a result, DRAs are almost completely removed from the FPP image.

volunteer. Each slice is reconstructed with full k-space (first column), left-sided k-space (second column) and right-sided k-space (third column). The results are consistent with what is observed in numerical simulations: Slice 1 has reduced DRA when right side of k-space is used, and has more severe DRA when left side of k-space is used. Conversely, Slice 2 and 3 have reduced DRA when left side of k-space is used, and have more severe DRA when right side of k-space is used. As another example for DRA reduction, Fig. 7 shows a frame from Slice 2 of a healthy volunteer. In this case example, DRAs can be globally observed throughout subendocardial border (shown with red arrows). The proposed method, however, reduces the severity of DRA to a great extent by using the optimal temporal window for that particular slice.

B. Volunteer Studies

Fig. 8 shows 3 representative cases for DRA detection. Case 1 is a healthy volunteer with DRAs in septal and inferior walls (shown with red arrows). Fig. 8a2 shows the corresponding pixel-wise "slope map" for Case 1. As can be seen, the regions with DRA have very high slope values indicated by yellow pixels. Fig. 8a3 shows the AHA segments with detected DRA after processing this slope map. The algorithm correctly classifies 4 myocardial segments with DRA. Case 2 corresponds to a patient with known distal LAD disease. The region shown with a green arrow is a true perfusion defect while the region shown with a red arrow is a DRA in the septal wall. In the corresponding slope map in Fig. 8b2, the region with DRA has significantly higher slope values than the rest of myocardium. After processing this slope map, 2 myocardial segments in the septal wall are correctly detected as having DRA. An important point to note here is that the myocardial sector which has a true perfusion defect has very low slope values as expected, and thus can easily be differentiated from DRA by our proposed algorithm. Finally, Case 3 is a patient with suspected heart failure with reduced ejection fraction. All the dark regions that are shown with green arrows in Fig. 8c1 are true perfusion defects and not DRA. As can be seen from the corresponding slope map (Fig. 8c2), the slope values throughout myocardium are noticeably small. As a result, none of the segments are detected as having DRA (Fig. 8c3).

C. Animal Studies

Fig. 9 shows the results from one of the canine studies with epicardial stenosis resulting in a large perfusion defect. The

Figure 6. **Example results from a healthy volunteer to demonstrate the different DRA-inducing motion characteristics for Slice 1 vs Slice 2-3 (using the slice-indexing convention shown in Fig 2).** Slice 1 is acquired in systole while Slice 2 and 3 are acquired in diastole. Consistent with the dynamic simulation, the part of k-space with minimal cardiac motion results in reduced DRA and vice versa. Namely, for Slice 1, using a left-sided temporal window results in worse DRA (a2) and a right-sided temporal window results in suppressed DRA (a3). For Slice 2 and 3, however, using a left-sided temporal window results in suppressed DRA (b2,c2) and right-sided window results in a worse/enhanced DRA (b3,c3).
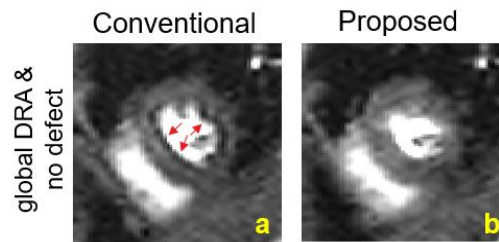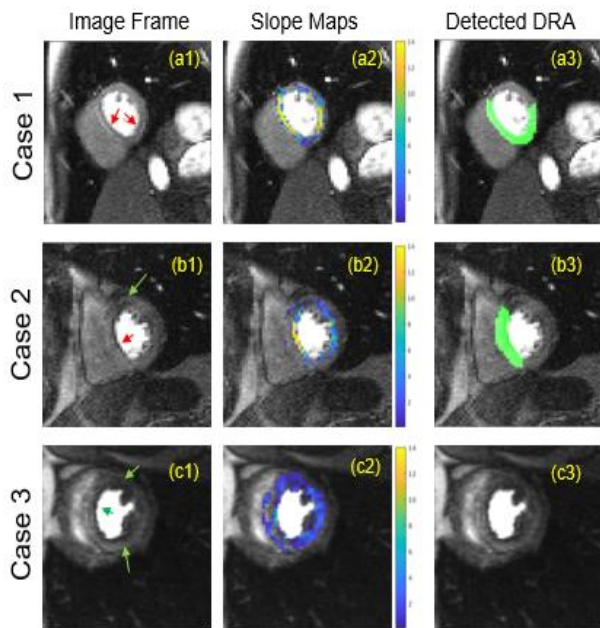
Figure 8. **Representative results from volunteer studies.** (a1) Case 1 shows a perfusion image frame from a healthy volunteer with DRA in septal and inferior wall of the heart (red arrows). As can be seen in (a2), the regions with DRA are highlighted by the algorithm in the slope map. (a3) shows detected myocardial segments after processing the slope map. (b1) Case 2 belongs to a patient with known distal LAD disease. The region in the septal wall is DRA (red arrow), and the region in anterior wall is a true perfusion defect (green arrow). (b2) shows the corresponding slope map. Note that only the septal wall with DRA has large slope values. (b3) shows the detected myocardial segments with DRA. (c1) Finally, Case 3 is a patient with suspected heart failure with reduced ejection fraction, and all the dark regions in myocardium are true perfusion defects (green arrows). (c2) shows the resulting slope map for Case 3. Unlike other cases with DRA, pixels have very small slope values. (c3) As there is not a sufficient number of large slope values in any myocardial segments, our algorithm (correctly) does not detect any segments as having DRA in this case.

dark region shown with green arrow in Fig. 9a is the hypoperfused area and not DRA. The region shown with red arrow, however, is a DRA. As shown in the slope map in Fig. 9b, the region with DRA has high slope values that are highlighted with yellow color. Other regions, on the other hand, do not have a noticeable batch of high-slope pixels. After the processing of this slope map, the septal myocardial segment with DRA can be correctly detected, as shown in Fig. 9c.

D. Detection Performance of the Proposed Algorithm

The artifact detection performance of the proposed method was assessed in the context of maximized specificity for detection of DRAs (i.e., to ensure no true perfusion defects are categorized as DRA). This setting is appropriate in clinical studies wherein the goal is to detect severe stress-induced perfusion deficits corresponding to obstructive coronary artery disease. In the examined set of FPP studies, we had a total of 47 myocardial slices. Optimizing the detection threshold for a specificity of 100% resulted in a sensitivity of 81% for per-slice DRA detection.
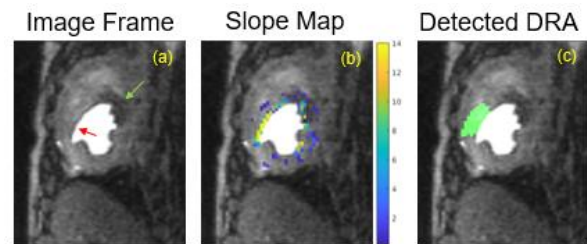

Figure 9. **Representative stress first-pass perfusion time frame (peak myocardial enhancement) from animal studies (canines with epicardial stenosis).** (a) An example frame that shows DRA (red arrow) and hypoperfused region (green arrow). (b) As can be seen from the slope map, the only region with very high slope values is the region with DRA. (c) Finally, the slope map can be processed to detect the myocardial segment with DRA.

IV. DISCUSSION

In this work, we proposed a new algorithm to detect motion-induced subendocardial DRA in first-pass perfusion cMRI images acquired with routine clinical protocols and Cartesian k-space sampling. Our algorithm takes advantage of deep-learning-based myocardial segmentation and automatically examines if a specific myocardial segment is likely to have DRA on the basis of the pixel-level signal intensity behavior when different temporal windows are used for image reconstruction. Experiments performed on patient volunteers (n=15) and canines (n=2) showed that our algorithm achieves per-slice performance of 81% sensitivity and 100% specificity for detection of subendocardial DRA.

The threshold values used in this work can be tuned experimentally so that an ideal specificity of 100% is achieved at the cost of reduced sensitivity. This approach for determining the detection threshold may be appropriate in the context of aiming to diagnose obstructive coronary artery disease which corresponds to severe stress-induced perfusion defects. In this setting, incorrectly classifying a segment which includes a true perfusion defect as DRA can result in underestimation of the severity of disease (ischemic burden), which can justify the need for having a 100% specific algorithm for DRA detection. It is important to note that, in a more general setting—e.g., if the diagnostic goal is different from obstructive coronary artery disease—a different threshold may be optimal.

An interesting byproduct of the proposed method is generating a series of alternative image reconstructions with truncated k-space (one-sided partial Fourier k-space coverage) from the same k-space data, some of which may have reduced DRA compared to the original reconstruction which uses the entire acquired k-space. As shown in Fig. 6, it is typically the case that a specific choice among the reconstructions with retrospectively-reduced temporal footprint (reconstructed using partial Fourier and parallel-imaging acceleration) has significantly suppressed subendocardial DRA—both in terms of extent and severity. This is simply due to the fact that by eliminating parts of the k-space with rapid motion, we are "shaping" the PSF induced by the cardiac motion effects to have a more ideal form. Although DRA reduction is not the main goal of this work, it can help increase the performance of quantitative/semi-quantitative methods used for analysis of

FPP cMRI datasets. Further work needs to be done in this area in future efforts.

A key feature of our proposed algorithm is that it can be applied to individual time frames in the FPP image series. This enables the end-user to evaluate which specific time frames are suspected of having DRA. Nevertheless, the detection performance of our algorithm improves if it is jointly applied across multiple frames. This is because DRA typically exhibits temporal correlations, e.g., if it is present in a specific myocardial segment and a specific time frame, it often persists in that myocardial segment for at least another 1 or 2 time frames, i.e., does not disappear immediately in the image series. A technical feature of our algorithm is that it does not need image-intensity normalization using so-called "proton density" images. Before finding the corresponding slope map, stacked frames from different realizations are normalized to the LV blood pool. This self-normalization process eliminates the need for a separate set of proton-density image, which not be available.

An important aspect that increases the robustness of our method is that it does not require an accurate myocardial segmentation. As described in Fig. 4, our method can eliminate the blood pixels/partial volume effects based on the prior information about the polarity of slope values for pixels with DRA. The polarity of DRA pixels is determined based on which cardiac cycle that particular slice is acquired in. After the clipping operation, pixels with DRA in the myocardium can be more precisely distinguished from the left ventricular blood pool.

A. Limitations

A limitation of this work is the need to determine a threshold value that can be applied to the slope maps for detection of DRA in each myocardial slice or segment. A specific threshold value will not be optimal for all clinical settings and may depend on the pulse sequence parameters. Therefore, the thresholds likely need to be adjusted depending on the clinical application and the specific pulse sequence used in the imaging protocol. Another limitation is that in data-acquisition protocols (pulse sequences) where spatial resolution is reduced to have a small temporal footprint (e.g., below 75 msec), the left-sided and right-sided k-space windows may not show sufficient distinction in the behavior of DRA. In such settings, the contribution of Gibbs ringing to the total DRA may become greater than the contribution of motion. In such cases, the proposed algorithm may have a lower sensitivity for detecting the regions with DRA.

B. Conclusions

To the best of our knowledge, our work is the first approach for performing automatic detection of the subendocardial dark-rim artifact in first-pass perfusion cMRI without the need for quantification of myocardial blood flow. Furthermore, our approach is the first to leverage the power of CNNs to automate the process of dark-rim artifact detection and suppression in perfusion cMRI. Future works include further evaluation of the performance by applying the technique in a wider patient population, and investigating the impact of image-artifact reduction in quantitative FPP cMRI.

REFERENCES

[1] P. Kellman and A. E. Arai, "Imaging sequences for first pass perfusion --a review," *J Cardiovasc Magn Reson,* vol. 9, no. 3, pp. 525-37, 2007.

[2] E. Nagel *et al.*, "Magnetic resonance perfusion measurements for the noninvasive detection of coronary artery disease," *Circulation,* vol. 108, no. 4, pp. 432-7, 2003.

[3] J. Schwitter *et al.*, "Assessment of myocardial perfusion in coronary artery disease by magnetic resonance: a comparison with positron emission tomography and coronary angiography," *Circulation,* vol. 103, no. 18, pp. 2230-5, 2001.

[4] N. M. Wilke, M. Jerosch-Herold, A. Zenovich, and A. E. Stillman, "Magnetic resonance first-pass myocardial perfusion imaging: clinical validation and future applications," *J Magn Reson Imaging,* vol. 10, no. 5, pp. 676-85, 1999.

[5] B. L. Gerber *et al.*, "Myocardial first-pass perfusion cardiovascular magnetic resonance: history, theory, and current state of the art," *J Cardiovasc Magn Reson,* vol. 10, p. 18, 2008.

[6] E. V. Di Bella, D. L. Parker, and A. J. Sinusas, "On the dark rim artifact in dynamic contrast-enhanced MRI myocardial perfusion studies," *Magn Reson Med,* vol. 54, no. 5, pp. 1295-9, 2005.

[7] M. Jerosch-Herold, "Quantification of myocardial perfusion by cardiovascular magnetic resonance," *J Cardiovasc Magn Reson,* vol. 12, p. 57, 2010.

[8] P. Storey, Q. Chen, W. Li, R. R. Edelman, and P. V. Prasad, "Band artifacts due to bulk motion," *Magn Reson Med,* vol. 48, no. 6, pp. 1028-36, 2002.

[9] P. Ferreira, P. Gatehouse, P. Kellman, C. Bucciarelli-Ducci, and D. Firmin, "Variability of myocardial perfusion dark rim Gibbs artifacts due to sub-pixel shifts," *J Cardiovasc Magn Reson,* vol. 11, p. 17, 2009.

[10] E. Kellner, B. Dhital, V. G. Kiselev, and M. Reisert, "Gibbs-ringing artifact removal based on local subvoxel-shifts," *Magn Reson Med,* vol. 76, no. 5, pp. 1574-1581, 2016.

[11] M. Salerno, C. Sica, C. M. Kramer, and C. H. Meyer, "Improved first-pass spiral myocardial perfusion imaging with variable density trajectories," *Magn Reson Med,* vol. 70, no. 5, pp. 1369-79, Nov 2013.

[12] B. Sharif *et al.*, "Towards elimination of the dark-rim artifact in first-pass myocardial perfusion MRI: removing Gibbs ringing effects using optimized radial imaging," *Magn Reson Med,* vol. 72, no. 1, pp. 124-36, Jul 2014. doi: 10.1002/mrm.24913

[13] Z. Zhou *et al.*, "First-pass myocardial perfusion MRI with reduced subendocardial dark-rim artifact using optimized Cartesian sampling," in *J Magn Reson Imaging* vol. 45, 2017, pp. 542-555. doi: 10.1002/jmri.25400

[14] A. D. Ta *et al.*, "Fully quantitative pixel-wise analysis of cardiovascular magnetic resonance perfusion improves discrimination of dark rim artifact from perfusion defects associated with epicardial coronary stenosis," *J Cardiovasc Magn Reson,* vol. 20, no. 1, p. 16, 2018.

[15] Sandoval Z, Van Dyke J, Dharmakumar R, Sharif B. Rapid Automatic Quantification of Myocardial Blood Flow in Free-breathing Myocardial Perfusion MRI without the Need for Motion Correction: A Novel Spatio-temporal Deep Learning Approach. Proceedings of ISMRM 2019;27:12.

[16] M. A. Griswold *et al.*, "Generalized autocalibrating partially parallel acquisitions (GRAPPA)," *Magn Reson Med,* vol. 47, no. 6, pp. 1202-10, 2002.